
Equivariant Multi-Modality Image Fusion

Zixiang Zhao^{1,2} Haowen Bai¹ Jianshe Zhang¹ Yulun Zhang² Kai Zhang²
Shuang Xu³ Dongdong Chen⁴ Radu Timofte^{2,5} Luc Van Gool²

¹Xi'an Jiaotong University ²Computer Vision Lab, ETH Zürich

³Northwestern Polytechnical University ⁴University of Edinburgh ⁵University of Würzburg

Abstract

Multi-modality image fusion is a technique used to combine information from different sensors or modalities, allowing the fused image to retain complementary features from each modality, such as functional highlights and texture details. However, effectively training such fusion models is difficult due to the lack of ground truth fusion data. To address this issue, we propose the Equivariant Multi-Modality imAge fusion (EMMA) paradigm for end-to-end self-supervised learning. Our approach is based on the prior knowledge that imaging function are equivariant to specific transformations. Thus, we introduce a novel training framework that includes a fusion module and a learnable pseudo-sensing module, which allow the network training to follow the principles of physical sensing and imaging process, and meanwhile satisfy the equivariant prior for natural images. Our extensive experiments demonstrate that our method produces high-quality fusion results for both infrared-visible and medical images, while facilitating downstream multi-modal segmentation and detection tasks. The code will be released.

1 Introduction

Multi-modality image fusion, as an image restoration technique that aggregates information from multiple sensors and modalities to generate a comprehensive representation of scenes and objects [1–4]. It finds widespread application in tasks such as image registration [5–7], scene information enhancement or restoration [8, 9], and downstream tasks such as object detection [10, 11] and semantic segmentation [12, 13] in scenes with multiple sensors. The most notable tasks include *infrared-visible image fusion* (IVF) and *medical image fusion* (MIF). IVF focuses on combining thermal radiation information from input infrared images and intricate texture details from input visible images, producing fusion images that overcome the limitations of visible images affected by illumination variations, and infrared images affected by low resolution and noise [14]. The primary goal of MIF is to provide a comprehensive representation of any abnormalities in a patient’s medical condition. This is achieved by integrating multiple imaging techniques, resulting in an intelligent decision-making system that supports both the diagnosis and treatment processes [15].

As an atypical image inverse problem, the most challenging difficulty of image fusion task lies in that each sensor can only capture its own modality features, and there is no “super” sensor that can perceive all modal information in real life. As a result, there is no ground truth for this task, making it difficult to effectively apply the powerful supervised learning paradigm of deep learning to fusion tasks. Despite this, numerous deep learning-based methods have attempted to solve this issue, with representative works being generative methods [11, 16] and manually-designed loss function methods [1, 3, 17]. Generative methods aim to produce a fused image that closely resembles the source images in distribution, through adversarial training [11] or latent variables modeling [18]. In contrast, methods with manually-designed loss functions hope to achieve effective end-to-end learning and preserve more original information by minimizing the distance between the fused image and source images in different feature domains, such as spatial [19], frequency [20], or gradient

domain [13]. However, generative methods often struggle to explicitly and effectively align the distributions and are prone to problems such as mode collapse and difficult training. Meanwhile, manually designed loss functions are often only tailored to specific modality characteristics and are difficult to effectively capture the distance or measures suitable for different modality images, resulting in poor generalization ability and flexibility.

As aligning distributions and manually designing loss functions are difficult to accomplish, we propose to begin with the physical imaging process and learn the perception or mapping from the fused image to different modality images, which is obviously simpler than learning the fusion process. In this way, we can calculate the loss between the input source images and the (pseudo) sensing results obtained by feeding fused images to different sensing functions, overcoming the issue of lacking ground truth fusion images.

Following this workflow, we propose a learnable pseudo-sensing module based on U-Net [21], which models the mapping from the fused image to the source images to simulate the physical perception imaging process. In addition, a U-Net-like fusion module named U-Fuser, consisting of Restormer [22]-CNN block as the basic unit, is used to model global-local features and effectively complete the information aggregation. Furthermore, since image fusion is an ill-posed problem, optimizing the above sensing loss does not necessarily result in the optimal fused image. Therefore, priors are introduced to constrain the solution space and obtain improved fusion results. In this paper, we utilized a conceptually simple yet effective prior that natural imaging responses are equivariant to translations like shift, rotations, and reflections. Based on the inherent properties of natural images, the equivariant prior can provide better constraints and guidance for the learning process of fusion network. Coupled with the learnable fusion module and pseudo sensing module, we devise our self-supervised learning paradigm named **Equivariant Multi-Modality imAge fusion (EMMA)**.

Our contributions are organized into four aspects:

- We propose a straightforward and effective self-supervised learning paradigm named EMMA, which overcomes the challenge of lacking ground truth in image fusion tasks. Our paradigm is based on the physical imaging process with the natural prior that imaging is equivariant to transformations such as shift, rotation, and reflection.
- We transform the conventional loss calculation in this task into simulating a perceptual imaging process. The learnable pseudo-sensing module and the sensing loss term in EMMA can inspire future researchers to develop models based on physical imaging.
- The U-Fuser fusion module proposed in EMMA can proficiently model long- and short-range dependencies at multiple scales and fuse the source information.
- Our approach has demonstrated excellent performance in infrared-visible image fusion and medical image fusion, which is also proved to facilitate downstream multi-modal object detection and semantic segmentation tasks.

2 Related Work

Multi-modality image fusion. In the deep learning era, multi-modality image fusion methods can be classified into four primary groups: generative models [16, 23, 24], autoencoder-based models [12, 17, 25, 26], algorithm unrolling models [19, 27–29], and unified models [1, 30–33]. Generative models represent the distribution of fused images and source images in the latent space through generative adversarial networks [16, 23, 24] or other generative models [18, 34]. By making the distribution of the fused image close to that of the source image, the fused image is obtained by sampling from the posterior probability of the former. Autoencoder-based models use the encoder/decoder with CNN or Transformer block as the basic unit to model the mapping/inverse mapping between the image domain and the feature domain [4, 9]. Algorithm unrolling models shift the algorithm focus from data-driven learning to model-driven learning. They replace complex operators in conventional optimization with CNN or Transformer blocks while retaining the original computational graph structure, achieving lightweight and interpretable learning [19]. Unified models identify meta-knowledge or meta-information between different tasks through cross-task learning, enabling rapid adaptation to new tasks and improved performance with fewer examples [1, 26].

Moreover, the multi-modality image fusion task is often integrated into coupled systems with upstream (pre-processing) image registration [5–7] and downstream object detection and semantic segmentation tasks [11, 13, 35]. Image registration can effectively eliminate image artifacts and unaligned areas,

enhance edge clarity and expand the perception field [5, 36]. Furthermore, gradient of the recognition loss in downstream tasks can effectively guide the production of the fused image [11, 13].

Equivariant Imaging. Equivariant imaging [37–39] is an emerging fully unsupervised imaging framework that exploits the group invariance present in signal distributions to learn a reconstruction function from partial measurement data alone. This is in contrast to traditional supervised learning methods, *i.e.*, learning with ground truth, which requires pairs of signals and associated measurements for training. The basic idea behind equivariant imaging is to use the fact that natural signals often have certain symmetries. For example, images are often translation invariant, meaning that they look the same if they are shifted around. With this invariance/symmetry prior, the whole imaging system (from sensing to reconstruction) is transformation equivariant. Under certain physical sensing conditions [40], the reconstruction function will be able to correctly reconstruct images that have been transformed around, even if it has never seen those images before. As a promising new approach to imaging and a new way to acquire and process images, equivariant imaging has been shown to be effective for a variety of linear inverse problems in imaging, including MRI image reconstruction [38], seismic imaging [41], single-photon image super-resolution [42], and single-pixel imaging [43]. This paper devotes to exploring the potential of equivariant imaging on a more challenging task, *i.e.*, non-linear and blind inverse problems in multi-modality image fusion.

Comparison with existing approaches. Existing methods focus more on generating a fused image that is close to the source images in some measure. In contrast, our method is based on the physical imaging process. The motivation for our training paradigm is that, when the fused image is perceived through a sensing module, the obtained imaging result can closely approximate the source image. Furthermore, other prior-based optimizations often necessitate domain knowledge based on data. However, in our framework, we only need to use the apparent invariant prior of natural images to accomplish self-supervised learning. In other words, the transformed fused image, after sensing and re-fused, should yield the same outcome as before sensing.

3 Method

In this section, we first provide the formalization of the model, which includes the sensing module and the fusion module, and give the model hypotheses for establishing the equivariant image fusion paradigm. Then, we take the IVF task as an example and present the implementation and details of the EMMA model. Other image fusion tasks can be analogously derived.

3.1 Problem Overview

In this context, i , v , and f refer to infrared, visible, and fused images, respectively, with $i \in \mathbb{R}^{HW}$, $v \in \mathbb{R}^{3HW}$, and $f \in \mathbb{R}^{3HW}$. We assume the existence of an information-rich f that contains multi-sensory and multi-modal information and needs to be predicted. However, there is no perception device in real life that can fully sense f up to now. Thus, as an unsupervised task, there is no ground truth for f . Therefore, we model the fusion process and the sensing process as follows:

$$f = \mathcal{F}(i, v) + n_f \Leftrightarrow i = \mathcal{A}_i(f) + n_i, v = \mathcal{A}_v(f) + n_v, \quad (1)$$

where $\mathcal{F}(\cdot, \cdot)$ represents the fusion model, while $\mathcal{A}_i(\cdot)$ and $\mathcal{A}_v(\cdot)$ represent the sensing model of i and v , *i.e.*, the infrared and RGB cameras, respectively. In the traditional image inverse problem $y = \mathcal{A}(x) + n$, where x and y are the ground truth image and the measurement, and the degradation operator $\mathcal{A}(\cdot)$ is known (such as the noise distribution in denoising tasks and the blur kernel in super-resolution tasks). However, in image fusion tasks, we cannot explicitly obtain \mathcal{A}_i and \mathcal{A}_v . Nevertheless, we can set them to be learnable, in order to simulate the perceptual process and assist the network in self-supervised learning.

3.2 Model hypothesis

To provide comprehensive sensing and fusion models and further support the subsequent introduction of our self-supervised fusion framework, we first need to establish some necessary hypotheses.

a) Measurement consistency. We assume that the fusion function $\mathcal{F}(\cdot, \cdot)$ maintains consistency within the measurement domain, that is

$$\mathcal{A}_i(\mathcal{F}(i, v)) = i, \mathcal{A}_v(\mathcal{F}(i, v)) = v. \quad (2)$$

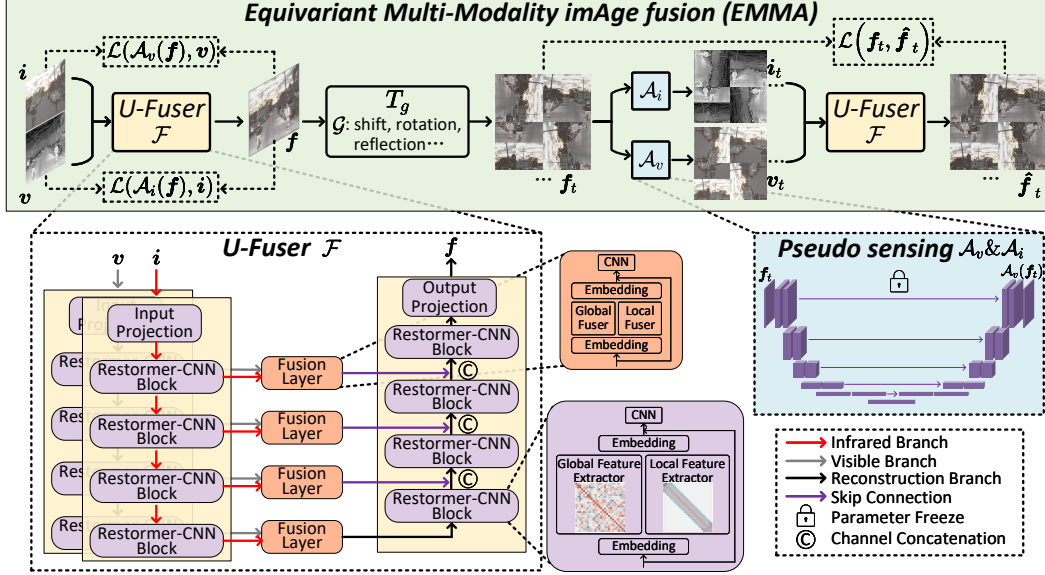


Figure 1: Workflow for EMMA. The image pair $\{i, v\}$ are initially input into U-Fuser \mathcal{F} , resulting in the fused image f . Next, a series of transformations T_g containing shift, rotation, reflection, *etc.*, are applied to f to produce f_t . f_t is then fed into the parameter-frozen $\{A_i, A_v\}$ to generate the pseudo-sensing images $\{i_t, v_t\}$, which are finally input into \mathcal{F} to obtain the re-fused image \hat{f}_t .

However, due to the underdetermined nature of the sensing process, the estimation of $\mathcal{F}(i, v)$ cannot be achieved by estimating the inverse of A_i or A_v , and we have to learn more information beyond the range space of their inverse.

b) Invariant set consistency. We first give two definitions in the equivariant imaging [37]:

Definition 1 (Invariant set). For a set of transformations $\mathcal{G} = \{g_1, \dots, g_{|\mathcal{G}|}\}$ composed of unitary matrices $T_g \in \mathbb{R}^{n \times n}$, \mathcal{X} is the invariant set with respect to transformations \mathcal{G} , if $T_g x \in \mathcal{X}$ holds for all $x \in \mathcal{X}$ and $g \in \mathcal{G}$. Additionally, $T_g \mathcal{X}$ and \mathcal{X} are identical while following the same distribution, i.e., $p(T_g x) = p(x)$.

Definition 2 (Equivariant function). If composition function $k \circ l$ satisfies $k \circ l(T_g x) = T_g k \circ l(x)$ for $\forall x \in \mathcal{X}$ and $\forall g \in \mathcal{G}$, we call $k \circ l$ the equivariant function with respect to the transformation \mathcal{G} .

For the deduction of Definition 1, if \mathcal{X} is a set of natural images, then it will be an invariant set, and naturally \mathcal{X} is an invariant set for transformations \mathcal{G} that contains shift, rotation and reflection transformations. Furthermore, as a subset of \mathcal{X} , the set composed of the fused images f is also equivariant to \mathcal{G} . Then we give the following theorem:

Theorem 1 (Equivariant image fusion hypothesis). If we regard k and l in Definition 2 as the fusion model \mathcal{F} and the sensing model \mathcal{A} (including A_i and A_v), we can obtain the equivariant image fusion hypothesis:

$$\mathcal{F}(A_i(T_g f), A_v(T_g f)) = T_g \mathcal{F}(A_i(f), A_v(f)). \quad (3)$$

Remark 1. For Eq. (3), it does not necessitate \mathcal{F} or \mathcal{A} to be equivariant to T_g , instead, $\mathcal{F} \circ \mathcal{A}$ is required to be equivariant. Thus, \mathcal{F} and \mathcal{A} here can be set to any form of mapping without restriction.

In the following section, we will demonstrate how to establish our self-supervised learning paradigm based on Theorem 1.

3.3 Self-supervised equivariant image fusion framework

The main focus of this paper is to present EMMA, a self-supervised image fusion framework based on the equivariant imaging prior, with the specific workflow shown in Fig. 1.

3.3.1 Overall paradigm

Firstly, we establish a U-Net-like fusion module $\mathcal{F}(\cdot)$ named *U-Fuser*, which combines a Restormer [22] with CNN blocks as the basic unit to generate the fused image \mathbf{f} from inputs \mathbf{i} and \mathbf{v} . Subsequently, based on the equivariant image fusion hypothesis in Theorem 1, an equivariant prior-based self-supervised framework, comprising *U-Fuser module* and learnable (*pseudo*) *sensing modules* \mathcal{A}_i and \mathcal{A}_v , is employed to better preserve the source image information in the absence of the fusion ground truth. Specifically, we transform \mathbf{f} , estimated by U-Fuser, through a series of transformations T_g to obtain \mathbf{f}_t , then pass \mathbf{f}_t through pseudo sensing modules $\{\mathcal{A}_i, \mathcal{A}_v\}$ to obtain pseudo-images $\{\mathbf{i}_t, \mathbf{v}_t\}$. Finally, we fuse $\{\mathbf{i}_t, \mathbf{v}_t\}$ with U-Fuser again to obtain $\hat{\mathbf{f}}_t$.

Unlike other methods that require a well-designed loss function to minimize the distance between \mathbf{f} and $\{\mathbf{i}, \mathbf{v}\}$, EMMA’s loss focuses on making the pseudo-images $\{\mathcal{A}_i(\mathbf{f}), \mathcal{A}_v(\mathbf{f})\}$ generated by the sensing module from \mathbf{f} as close to the original $\{\mathbf{i}, \mathbf{v}\}$ as possible, while making \mathbf{f}_t close to $\hat{\mathbf{f}}_t$ simultaneously. Thus, from a physical imaging perspective, the optimal fusion image \mathbf{f} is found.

In the following text, we will first introduce two important components of the EMMA, *i.e.*, the fusion module U-Fuser and the pseudo sensing modules $\{\mathcal{A}_i, \mathcal{A}_v\}$, then illustrate the entire self-supervised learning framework, and finally provide the training loss function.

3.3.2 Stage I: U-Fuser module learning

We first train U-Fuser $\mathcal{F}(\cdot)$ for fusing \mathbf{i} and \mathbf{v} and generating the fused image \mathbf{f} . To model features at different scales, we adopt a U-Net-like structure for feature extraction and reconstruction. At each scale, since the input cross-modal features contain both global features such as environment and background information, as well as local features like the highlighting and detailed texture object features, we design a Transformer-CNN structure to better model the cross-modal features by leveraging their respective inductive biases.

For the selection of the Transformer block, we adopt the Restormer block in [22], which implements self-attention in the channel dimension to model global features without too much computation load. In the CNN block, we use the Res-block [44] structure. The input features of the Restormer-CNN block are embedded and then parallelly processed by the Restormer block and the Res-block, followed by embedding interaction and a CNN layer, and finally input to the next scale. Features of \mathbf{i} and \mathbf{v} at the same scale are fused in the fusion layer, and are passed to the reconstruction branch at the previous scale via skip connections. The designs of blocks for feature fusion and reconstruction are the same as the Restormer-CNN block used in the feature extraction branch.

3.3.3 Stage II: Pseudo sensing module learning

In contrast to other works in this field where their algorithm mainly focuses on the design of the fusion function \mathcal{F} , in this paper, we propose a self-supervised learning framework based on equivariant imaging prior to address the issue of lacking ground truth for fused images. According to the equivariant image fusion hypothesis stated in Theorem 1, we need to obtain pseudo imaging results from $\mathcal{A}_i(\mathbf{f})$ and $\mathcal{A}_v(\mathbf{f})$. To achieve this goal, we need to simulate the process of sensing infrared and visible images from the (imagined) fused image, as described in Eq. (2). Since it is not feasible to explicitly give the structures of \mathcal{A}_i and \mathcal{A}_v , we adopt a data-driven learning approach to obtain them. Recently, many deep learning-based methods have shown promising results in image fusion. Therefore, we selected nine state-of-the-art (SOTA) methods that have recently appeared in top venues. They are DIDFuse [3], U2Fusion [1], SDNet [26], RFN-Nest [17], AUIF [19], RFNet [5], TarDAL [11], DeFusion [9] and ReCoNet [36]. We use their fusion results as the (pseudo) ground truth for the fused images and then learn the mappings from the fused images to \mathbf{i} and \mathbf{v} , which can be regarded as \mathcal{A}_i and \mathcal{A}_v , respectively. Considering that both the input and output of the mapping have the same image size, we choose U-Net [21] as the backbone of \mathcal{A}_i and \mathcal{A}_v and conduct the end-to-end training paradigm. The specific network details can be found in the supplementary material.

3.3.4 Stage III: Equivariant fusion

After obtaining the U-Fuser \mathcal{F} and pseudo-sensing functions $\{\mathcal{A}_i, \mathcal{A}_v\}$, we introduce a self-supervised learning framework based on imaging equivariant prior. As shown in Fig. 1, we first input the image pairs $\{\mathbf{i}, \mathbf{v}\}$ into \mathcal{F} , and obtain fused image \mathbf{f} (which is the entire operation of conventional fusion

algorithms). Then, we apply a series of transformations T_g to \mathbf{f} , including shift, rotation, reflection *etc.*, to obtain \mathbf{f}_t . Subsequently, \mathbf{f}_t is input into the well-trained $\{\mathcal{A}_i, \mathcal{A}_v\}$ to obtain the pseudo-sensing images $\{\mathbf{i}_t, \mathbf{v}_t\}$, which contain the information from \mathbf{f}_t and satisfy the imaging characteristics of infrared and visible images, respectively. Finally, paired $\{\mathbf{i}_t, \mathbf{v}_t\}$ are fed into \mathcal{F} to obtain the re-fused image $\hat{\mathbf{f}}_t$. Throughout the framework, we aim to aggregate information from $\{\mathbf{i}, \mathbf{v}\}$ into \mathbf{f} , and according to the equivariant image fusion hypothesis (Theorem 1), \mathbf{f}_t and $\hat{\mathbf{f}}_t$ should be sufficiently close. These will be guaranteed through the designed loss function.

3.3.5 Training detail and loss function

During the entire training process of EMMA, we first trained \mathcal{A}_i and \mathcal{A}_v using ℓ_1 loss as the loss function, *i.e.*, $\mathcal{L}_I^{Rec} = \ell_1(\mathbf{i}, \mathcal{A}_i(\tilde{\mathbf{f}}))$ and $\mathcal{L}_V^{Rec} = \ell_1(\mathbf{v}, \mathcal{A}_v(\tilde{\mathbf{f}}))$, where $\tilde{\mathbf{f}}$ are the fusion results from the SOTA methods in Sec. 3.3.3. Then, we freeze the parameters of \mathcal{A}_i and \mathcal{A}_v , which means that the parameters of the pseudo-sensing module will no longer be updated. Afterwards, we train the U-Fuser module with the total loss function:

$$\arg \min_{\theta} \mathbb{E}_{\mathbf{i}, \mathbf{v}, g} \mathcal{L}(\mathcal{A}_i(\mathbf{f}), \mathbf{i}) + \alpha_1 \mathcal{L}(\mathcal{A}_v(\mathbf{f}), \mathbf{v}) + \alpha_2 \mathcal{L}(\mathbf{f}_t, \hat{\mathbf{f}}_t), \quad (4)$$

where $\mathcal{L}(\mathbf{x}, \hat{\mathbf{x}}) = \ell_1(\mathbf{x}, \hat{\mathbf{x}})$, α_1 and α_2 are the tuning parameters. In particular, the first and second terms of Eq. (4) ensure our paradigm satisfies Definition 1, while the third term ensures it satisfies Definition 2.

3.4 Explanations

Here we will explain why the unsupervised fusion of EMMA works. By the fact that image set $\{\mathbf{f}\}$ is invariant to a group of invertible transformations $\{T_g\}$, give any image \mathbf{f} from the invariant set $\{\mathbf{f}\}$, then $T_g\mathbf{f}$ also belongs to the set for all $g = 1, \dots, |G|$. Under the equivariant hypothesis in Theorem 1, we have $\{\mathbf{i}, \mathbf{v}\} = \mathcal{A}\mathbf{f} = \mathcal{A}T_gT_g^{-1}\mathbf{f} = \mathcal{A}_g\mathbf{f}'$ for $g = 1, \dots, |G|$, where $\mathcal{A}_g = \mathcal{A}T_g$ and $\mathbf{f}' = T_g^{-1}\mathbf{f}$ belongs to $\{\mathbf{f}\}$. That is to say, applying transformations is equal to generating multiple virtual sensing operators $\{\mathcal{A}_g\}_{g=1, \dots, |G|}$. Since those virtual operators \mathcal{A}_g are with potentially different nullspaces, this allows us to learn beyond the range space of inverse \mathcal{A} (see [40]). More details can be found in the supplementary material.

4 Experiment

In this section, we conducted numerous experiments to demonstrate the superiority of our approach and training paradigm.

4.1 Infrared and visible image fusion

Setup. We conduct experiments on four fashion benchmarks: MSRS [45], RoadScene [30], M³FD [11] and TNO [46]. The network is trained on the MSRS training set and tested on its test set to evaluate the performance. In addition, the trained model is implemented to RoadScene, M³FD and TNO without fine-tuning to verify the generalization performance. Our experiments are performed using PyTorch on a computer equipped with two NVIDIA GeForce RTX 3090 GPUs. The training image pairs are cropped into 128×128 patches randomly and with a batchsize of 8 before being fed into the network. α_1 and α_2 in Eq. (4) are set to 1 and 10, to ensure comparable magnitudes among the terms in the loss function. We train the network for 100 epochs using the Adam optimizer, with an initial learning rate of 1e-4 and decreasing by a factor of 0.5 every 20 epochs. U-Fuser is set to contain a four-layer structure with feature channels of [16, 32, 64, 128] in each layer. \mathcal{A}_i and \mathcal{A}_v are set as six-layer U-Nets [21]. They are pre-trained and parameter-frozen prior to the U-Fuser training. As for the transformation set \mathcal{G} , we will discuss it in our supplementary material.

4.1.1 Comparison with SOTA methods

We compare our method with other SOTA methods of IVF, including DIDFuse [3], U2Fusion [1], SDNet [26], RFNet [5], TarDAL [11], DeFusion [9] and ReCoNet [36]. Six metrics are used to objectively compare fusion performance, including entropy (EN), standard deviation (SD), average

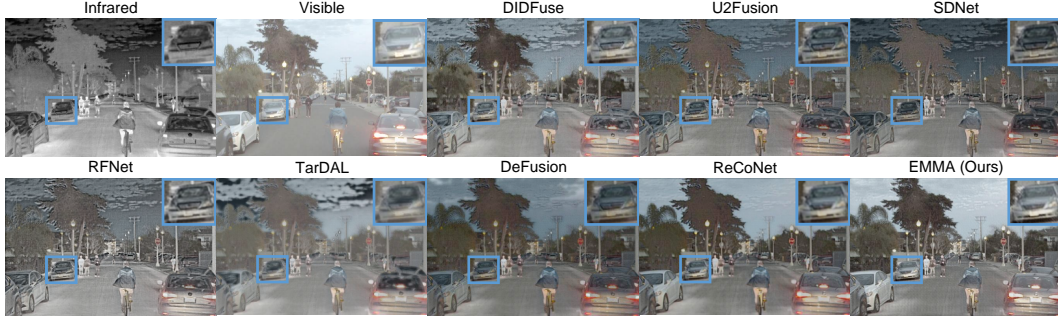


Figure 2: Visual comparison of “06832” from RoadScene [30] IVF dataset.

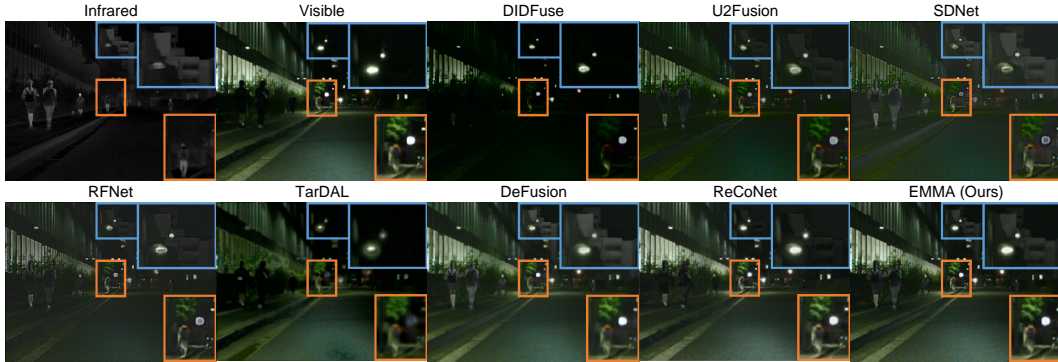


Figure 3: Visual comparison of “01282N” from MSRS [45] IVF dataset.

gradient (AG), mutual information (MI), visual information fidelity (VIF) and $Q^{AB/F}$, where higher values indicate superior fusion effects and calculation details are in [47].

Qualitative comparison. We compare the fusion outcomes of EMMA with SOTAs in Figs. 2 and 3. Our results successfully integrate thermal radiation information derived from infrared images with detailed texture features extracted from visible images. Fig. 2 demonstrates that the fused image accurately captures the advantages of each modality while eliminating redundant information. The fusion process enhances object visibility, sharpens textures, and reduces artifacts. In Fig. 3, objects situated in inadequately illuminated surroundings are prominently highlighted with well-defined edges and abundant contours. This distinctiveness facilitates the differentiation between foreground objects and the background, thereby enhancing our comprehension of the depicted scene.

Quantitative comparison. The fusion outcomes are quantitatively compared using six metrics, as shown in Tab. 1. Our method exhibits remarkable performance across nearly all metrics, affirming its suitability for various environmental conditions and object categories. Particularly noteworthy are the exceptional values obtained for SD, MI and VIF across all datasets. They indicate the capability of EMMA to produce images that align with human visual perception while preserving the integrity of the source image features and producing informative fused images.

4.1.2 Ablation studies

Terms in loss function. In Exp. I, we eliminate the last term in Eq. (4), which is the equivariant term. Even though the fusion module is capable of completing image fusion, it is unable to constrain the solution space through the equivariant prior. Thus, the network yields weaker results. In Exp. II, we modified the first two terms of Eq. (4) to be $\ell_1(\mathbf{f}, \mathbf{i}) + \ell_1(\mathbf{f}, \mathbf{v})$, which is the traditional loss in other fusion tasks. The first two terms of Eq. (4), *i.e.*, sensing loss, guarantee that the fused image needs to inherit enough information from source images, so that the output pseudo-perceptual imaging result can be closer to the source images. While the traditional loss function purely forces the fused image to closely resemble the source images. Results in Exp. II demonstrate the necessity of sensing loss term. In Exp. III, we replace the loss in Eq. (4) with that in Exp. II. The results indicate that without

Table 1: Quantitative results of IVF task. Best and second-best values are **highlighted** and underlined.

| | Dataset: MSRS Fusion Dataset [45] | | | | | | Dataset: M ³ FD Fusion Dataset [11] | | | | | | |
|-----------|-----------------------------------|--------------|-------------|-------------|-------------|-------------|--|-------------|--------------|-------------|-------------|-------------|-------------|
| | EN ↑ | SD ↑ | AG ↑ | MI ↑ | VIF ↑ | Qabf ↑ | EN ↑ | SD ↑ | AG ↑ | MI ↑ | VIF ↑ | Qabf ↑ | |
| DID [3] | 4.27 | 31.49 | 2.11 | 1.61 | 0.31 | 0.20 | DID [3] | 7.18 | 46.71 | 4.78 | 1.65 | <u>0.64</u> | 0.41 |
| U2F [1] | 5.37 | 25.52 | 2.82 | 1.40 | 0.54 | 0.42 | U2F [1] | 6.94 | 35.81 | 4.84 | 1.32 | 0.60 | <u>0.44</u> |
| SDN [26] | 5.25 | 17.35 | 2.67 | 1.19 | 0.50 | 0.38 | SDN [26] | 6.73 | 33.96 | 4.72 | 1.53 | 0.58 | 0.44 |
| RFN [5] | 5.56 | 24.09 | <u>3.53</u> | 1.30 | 0.51 | 0.43 | RFN [5] | 6.93 | 35.12 | 6.25 | 1.18 | 0.53 | 0.39 |
| TarD [11] | 5.28 | 25.22 | 1.83 | 1.49 | 0.42 | 0.18 | TarD [11] | 6.96 | <u>47.00</u> | 3.20 | <u>1.83</u> | 0.55 | 0.32 |
| DeF [9] | 6.46 | 37.63 | 2.80 | <u>2.16</u> | <u>0.77</u> | <u>0.54</u> | DeF [9] | 7.00 | 39.59 | 3.36 | 1.82 | 0.63 | 0.42 |
| ReC [36] | 6.61 | <u>43.24</u> | 3.46 | 2.16 | 0.71 | 0.50 | ReC [36] | <u>7.20</u> | 46.62 | 3.89 | 1.74 | 0.59 | 0.40 |
| Ours | <u>6.57</u> | 43.70 | 3.55 | 2.86 | 0.90 | 0.59 | Ours | 7.24 | 47.54 | <u>4.96</u> | 2.10 | 0.70 | 0.47 |

| | Dataset: RoadScene Fusion Dataset [30] | | | | | | Dataset: TNO Fusion Dataset [46] | | | | | | |
|-----------|--|--------------|-------------|-------------|-------------|-------------|----------------------------------|-------------|--------------|-------------|-------------|-------------|-------------|
| | EN ↑ | SD ↑ | AG ↑ | MI ↑ | VIF ↑ | Qabf ↑ | EN ↑ | SD ↑ | AG ↑ | MI ↑ | VIF ↑ | Qabf ↑ | |
| DID [3] | <u>7.39</u> | 51.96 | 6.11 | 2.07 | <u>0.57</u> | 0.45 | DID [3] | 6.99 | <u>45.42</u> | 5.12 | 1.95 | <u>0.63</u> | 0.47 |
| U2F [1] | 7.10 | 39.59 | 5.90 | 1.84 | 0.52 | 0.46 | U2F [1] | 6.80 | 32.41 | 4.92 | 1.66 | <u>0.63</u> | <u>0.55</u> |
| SDN [26] | 7.24 | 43.37 | 5.95 | 2.22 | 0.53 | <u>0.46</u> | SDN [26] | 6.76 | 34.17 | 4.81 | 2.05 | 0.53 | 0.52 |
| RFN [5] | 7.23 | 44.11 | 7.50 | 1.68 | 0.47 | 0.41 | RFN [5] | 6.75 | 32.53 | 7.01 | 1.58 | 0.57 | 0.50 |
| TarD [11] | 7.25 | 47.00 | 4.05 | 2.25 | 0.52 | 0.38 | TarD [11] | 6.75 | 40.42 | 2.82 | 2.22 | 0.51 | 0.29 |
| DeF [9] | 7.30 | 45.81 | 4.45 | 2.16 | 0.55 | 0.44 | DeF [9] | <u>7.01</u> | 39.11 | 3.13 | <u>2.30</u> | 0.57 | 0.41 |
| ReC [36] | 7.39 | <u>54.61</u> | 5.26 | <u>2.29</u> | 0.57 | 0.42 | ReC [36] | 6.90 | 38.54 | 3.95 | 2.16 | 0.57 | 0.48 |
| Ours | 7.45 | 56.38 | <u>6.92</u> | 2.42 | 0.62 | 0.43 | Ours | 7.21 | 45.52 | <u>5.22</u> | 3.04 | 0.83 | 0.68 |

Table 2: Ablation experiment results. **Highlighted** values indicate the best values.

| | Configurations | | | | EN | SD | AG | MI | VIF | Qabf |
|----------|----------------|------------------|------------------|-----------------|-------------|--------------|-------------|-------------|-------------|-------------|
| | Sensing Loss | Equivariant Loss | Global Extractor | Local Extractor | | | | | | |
| Exp. I | ✓ | | ✓ | ✓ | 6.36 | 39.22 | 3.01 | 1.96 | 0.72 | 0.55 |
| Exp. II | | ✓ | ✓ | ✓ | 6.42 | 40.12 | 3.29 | 1.97 | 0.79 | 0.55 |
| Exp. III | | | ✓ | ✓ | 6.21 | 38.96 | 2.99 | 1.77 | 0.76 | 0.52 |
| Exp. IV | ✓ | ✓ | | ✓ | 6.45 | 39.37 | 3.24 | 2.18 | 0.81 | 0.56 |
| Exp. V | ✓ | ✓ | ✓ | | 6.52 | 40.49 | 2.82 | 2.29 | 0.82 | 0.57 |
| Ours | ✓ | ✓ | ✓ | ✓ | 6.57 | 43.70 | 3.55 | 2.86 | 0.90 | 0.59 |

equivariant loss and sensing loss, relying on $\ell_1(\mathbf{f}, \mathbf{i}) + \ell_1(\mathbf{f}, \mathbf{v})$ loss makes it difficult to achieve an ideal fusion network.

U-Fuser. In Exp. IV and Exp. V, we separately eliminated the Restormer-block or the Res-block, ensuring consistent number of parameter by increasing the remaining blocks number. The results demonstrate that an incomplete feature extraction module leads to deficiencies in modeling local texture details or capturing long-range dependencies, thereby resulting in a degradation of performance.

4.2 Downstream IVF applications

This section aims to examine the impact of image fusion on downstream vision tasks. We assess the performance of fusion results in both *multi-modal semantic segmentation* (MMSS) tasks and *multi-modal object detection* (MMOD) tasks. To ensure fairness, we individually re-train the network for each task using fusion results obtained from their own methods. Due to space limitations, the visual comparisons are placed in the supplementary material.

4.2.1 Infrared-visible object detection

Setup. The MMOD task is conducted on the M³FD dataset [11], which comprises 4,200 images encompassing six categories of labels: people, cars, buses, motorcycles, trucks, and lamps. We partition the M³FD dataset into training/validation/test sets in an 8:1:1 ratio. The YOLOv5 detector [48] is trained using the SGD optimizer for 400 epochs. The batch size is set to 8, and the initial learning rate is set to 1e-2. We evaluate the detection performance by comparing the mAP@0.5.

Comparison with SOTA methods. The information presented in Tab. 3 indicates that EMMA exhibits the most superior detection capabilities, showcasing its ability to enhance the accuracy of detection by merging thermal radiation and RGB information and emphasizing hard-to-detect objects.

Table 3: AP@0.5(%) for MM detection.

| | Bus | Car | Lam | Mot | Peo | Tru | mAP@0.5 |
|------|-------------|-------------|-------------|-------------|-------------|-------------|-------------|
| IR | 78.8 | 88.7 | 70.2 | 63.4 | 80.9 | 65.8 | 74.6 |
| VI | 78.3 | 90.7 | 86.4 | 69.3 | 70.5 | 70.9 | 77.7 |
| DID | 79.7 | 92.5 | 84.7 | 68.7 | 79.6 | 68.8 | 79.0 |
| U2F | 79.2 | 92.3 | 87.6 | 66.8 | 80.7 | 71.4 | 79.6 |
| SDN | 81.4 | 92.3 | 84.1 | 67.4 | 79.4 | 69.3 | 79.0 |
| RFN | 78.2 | 91.9 | 85.0 | <u>72.8</u> | 79.4 | 69.0 | 79.4 |
| TarD | 81.3 | 94.8 | 87.1 | 69.3 | <u>81.5</u> | 68.7 | 80.5 |
| DeF | <u>82.9</u> | 92.5 | 87.8 | 69.5 | 80.8 | <u>71.4</u> | <u>80.8</u> |
| ReC | 78.9 | 91.8 | 87.4 | 69.3 | 79.4 | 70.0 | 79.5 |
| Ours | 83.2 | <u>93.5</u> | <u>87.7</u> | 77.7 | 82.0 | 73.5 | 82.9 |

Table 4: IoU(%) for MM segmentation.

| | Unl | Car | Per | Bik | Cur | CS | GD | CC | Bu | mIOU |
|------|-------------|-------------|-------------|-------------|-------------|-------------|-------------|-------------|-------------|-------------|
| IR | 90.5 | 75.6 | 45.4 | 59.4 | 37.2 | 51.0 | 46.4 | 43.5 | 50.2 | 55.4 |
| VI | 84.7 | 67.8 | 56.4 | 51.8 | 34.6 | 39.3 | 42.2 | 40.2 | 48.4 | 51.7 |
| DID | 97.2 | 78.3 | 58.7 | 60.9 | 36.2 | <u>52.9</u> | 62.4 | 44.0 | 55.7 | 60.7 |
| U2F | <u>97.5</u> | 82.3 | <u>63.4</u> | 62.6 | 40.3 | <u>52.6</u> | 51.9 | 44.8 | 59.5 | <u>61.7</u> |
| SDN | 97.3 | 78.4 | 62.5 | 61.7 | 35.7 | 49.3 | 52.4 | 42.2 | 52.9 | 59.2 |
| RFN | 97.3 | 78.7 | 60.6 | 61.3 | 36.3 | 49.4 | 45.6 | 45.7 | 48.0 | 58.1 |
| TarD | 97.1 | 79.1 | 55.4 | 59.0 | 33.6 | 49.4 | 54.9 | 42.6 | 53.5 | 58.3 |
| DeF | 97.5 | <u>82.6</u> | 61.1 | <u>62.6</u> | 40.4 | 51.5 | 48.1 | <u>47.9</u> | 54.8 | 60.7 |
| ReC | 97.4 | 81.0 | 59.9 | 61.4 | <u>41.0</u> | 51.3 | 54.4 | 47.4 | 55.9 | 61.1 |
| Ours | 97.6 | 84.0 | 65.2 | 63.1 | 42.4 | 53.6 | <u>60.2</u> | 50.5 | <u>56.3</u> | 63.7 |

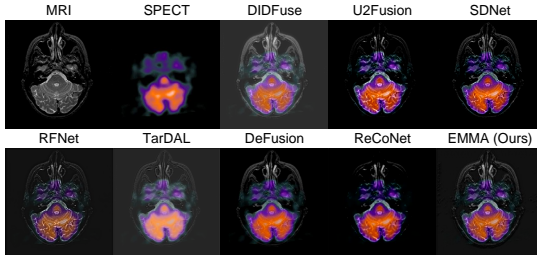


Figure 4: Visual comparison for MIF task.

Dataset: Harvard Medical Fusion Dataset [50]

| | EN \uparrow | SD \uparrow | AG \uparrow | MI \uparrow | VIF \uparrow | Qabf \uparrow |
|------|---------------|---------------|---------------|---------------|----------------|-----------------|
| DID | 4.39 | 29.08 | 3.42 | 1.42 | 0.40 | 0.27 |
| U2F | 3.47 | 52.29 | 5.10 | 1.57 | 0.48 | 0.55 |
| SDN | 3.44 | 50.55 | 5.83 | 1.57 | 0.55 | 0.66 |
| RFN | 4.42 | 43.77 | <u>6.28</u> | 1.45 | 0.45 | 0.58 |
| TarD | <u>4.43</u> | 55.95 | 4.04 | <u>1.66</u> | 0.56 | 0.40 |
| DeF | 3.82 | 57.41 | 4.65 | 1.65 | 0.64 | 0.61 |
| ReC | 3.34 | 62.02 | 5.41 | 1.42 | 0.50 | 0.57 |
| Ours | 5.18 | <u>58.76</u> | 6.40 | 1.71 | 0.64 | 0.73 |

Table 5: Quantitative results of MIF task.

4.2.2 Infrared-visible semantic segmentation

Setup. MSRS dataset [45] is designed for MMSS task and encompasses nine categories of pixel-level labels: background, bump, color cone, guardrail, curve, bike, person, car stop, and car. We select DeeplabV3+ [49] as the segmentation network and value the performances via Intersection over Union (IoU). The division of training and test sets adheres to the protocol in the original dataset paper [45]. We employ the cross-entropy loss along with the SGD optimizer. The total number of epochs is 340 while the backbone is frozen for the first 100 epochs. The batch size and the initial learning rate are set to 8 and $7e-3$, and the learning rate follows cosine annealing delayed as the epoch number increases.

Comparison with SOTA methods. Segmentation outcomes are displayed in Tab. 4. EMMA effectively combines the edge and contour details present in the source images, thereby improving the model’s capability to recognize the object’s boundary, and leading to more precise segmentation.

4.3 Medical image fusion

Setup. We conducted medical image fusion experiments via the Harvard Medical dataset [50], which included 50 pairs of MRI-CT/MRI-PET/MRI-SPECT images. We will directly generalize the models trained on the IVF task to the MIF task without fine-tuning. The quantitative metrics used are the same as those employed in the IVF task.

Comparison with SOTA methods. In both visual perception and quantitative measures in Fig. 4 and Tab. 5, EMMA demonstrates superior accuracy in extracting structural highlights and detailed texture features, and effectively integrates characteristic features within the fused image. Consequently, it achieves remarkable fusion results.

5 Conclusion

This paper addresses the challenge for the absence of ground truth in image fusion tasks by employing a conceptually simple yet effective prior that natural imaging responses are equivariant to translations such as shifts, rotations and reflections. Building upon this prior, we propose a self-supervised learning paradigm called equivariant image fusion. Furthermore, we adjust the inherent patterns of the loss function in this task by considering the principles of physical imaging, and transform the conventional loss calculation into simulating a perceptual imaging process. Additionally, we introduce a U-Net-like fusion module that utilizes the Restormer-CNN block as its basic unit, enabling improved extraction of global-local features and promoting efficient information fusion. The

experimental results demonstrate the effectiveness of our paradigm in multi-modality image fusion and its facilitation for downstream tasks such as multi-modality segmentation and detection.

References

- [1] Han Xu, Jiayi Ma, Junjun Jiang, Xiaojie Guo, and Haibin Ling. U2fusion: A unified unsupervised image fusion network. *IEEE Trans. Pattern Anal. Mach. Intell.*, 44(1):502–518, 2022.
- [2] Bikash Meher, Sanjay Agrawal, Rutuparna Panda, and Ajith Abraham. A survey on region based image fusion methods. *Information Fusion*, 48:119–132, 2019.
- [3] Zixiang Zhao, Shuang Xu, Chunxia Zhang, Junmin Liu, Jianshe Zhang, and Pengfei Li. DIDFuse: Deep image decomposition for infrared and visible image fusion. In *International Joint Conference on Artificial Intelligence, IJCAI*, pages 970–976, 2020.
- [4] Zixiang Zhao, Haowen Bai, Jianshe Zhang, Yulun Zhang, Shuang Xu, Zudi Lin, Radu Timofte, and Luc Van Gool. Cddfuse: Correlation-driven dual-branch feature decomposition for multi-modality image fusion. *CoRR*, abs/2211.14461, 2022.
- [5] Han Xu, Jiayi Ma, Jiteng Yuan, Zhuliang Le, and Wei Liu. Rfnnet: Unsupervised network for mutually reinforcing multi-modal image registration and fusion. In *CVPR*, pages 19647–19656. IEEE, 2022.
- [6] Di Wang, Jinyuan Liu, Xin Fan, and Risheng Liu. Unsupervised misaligned infrared and visible image fusion via cross-modality image generation and registration. In *IJCAI*, pages 3508–3515. ijcai.org, 2022.
- [7] Zhiying Jiang, Zengxi Zhang, Xin Fan, and Risheng Liu. Towards all weather and unobstructed multi-spectral image stitching: Algorithm and benchmark. In *ACM Multimedia*, pages 3783–3791, 2022.
- [8] Zixiang Zhao, Jianshe Zhang, Shuang Xu, Zudi Lin, and Hanspeter Pfister. Discrete cosine transform network for guided depth map super-resolution. In *Proceedings of the IEEE/CVF Conference on Computer Vision and Pattern Recognition (CVPR)*, pages 5697–5707, June 2022.
- [9] Pengwei Liang, Junjun Jiang, Xianming Liu, and Jiayi Ma. Fusion from decomposition: A self-supervised decomposition approach for image fusion. In *European Conference on Computer Vision (ECCV)*, 2022.
- [10] Alexey Bochkovskiy, Chien-Yao Wang, and Hong-Yuan Mark Liao. Yolov4: Optimal speed and accuracy of object detection. *CoRR*, abs/2004.10934, 2020.
- [11] Jinyuan Liu, Xin Fan, Zhanbo Huang, Guanyao Wu, Risheng Liu, Wei Zhong, and Zhongxuan Luo. Target-aware dual adversarial learning and a multi-scenario multi-modality benchmark to fuse infrared and visible for object detection. In *CVPR*, pages 5792–5801. IEEE, 2022.
- [12] Risheng Liu, Zhu Liu, Jinyuan Liu, and Xin Fan. Searching a hierarchically aggregated fusion architecture for fast multi-modality image fusion. In *ACM Multimedia*, pages 1600–1608. ACM, 2021.
- [13] Linfeng Tang, Jiteng Yuan, and Jiayi Ma. Image fusion in the loop of high-level vision tasks: A semantic-aware real-time infrared and visible image fusion network. *Inf. Fusion*, 82:28–42, 2022.
- [14] Xingchen Zhang and Yiannis Demiris. Visible and infrared image fusion using deep learning. *IEEE Transactions on Pattern Analysis and Machine Intelligence*, pages 1–20, 2023.
- [15] Alex Pappachen James and Belur V. Dasarathy. Medical image fusion: A survey of the state of the art. *Inf. Fusion*, 19:4–19, 2014.
- [16] Jiayi Ma, Wei Yu, Pengwei Liang, Chang Li, and Junjun Jiang. FusionGAN: A generative adversarial network for infrared and visible image fusion. *Information Fusion*, 48:11–26, 2019.
- [17] Hui Li, Xiao-Jun Wu, and Josef Kittler. Rfn-nest: An end-to-end residual fusion network for infrared and visible images. *Inf. Fusion*, 73:72–86, 2021.
- [18] Zixiang Zhao, Haowen Bai, Yuanzhi Zhu, Jianshe Zhang, Shuang Xu, Yulun Zhang, Kai Zhang, Deyu Meng, Radu Timofte, and Luc Van Gool. DDFM: denoising diffusion model for multi-modality image fusion. *CoRR*, abs/2303.06840, 2023.
- [19] Zixiang Zhao, Shuang Xu, Jianshe Zhang, Chengyang Liang, Chunxia Zhang, and Junmin Liu. Efficient and model-based infrared and visible image fusion via algorithm unrolling. *IEEE Trans. Circuits Syst. Video Technol.*, 32(3):1186–1196, 2022.

- [20] Man Zhou, Hu Yu, Jie Huang, Feng Zhao, Jinwei Gu, Chen Change Loy, Deyu Meng, and Chongyi Li. Deep fourier up-sampling. In *NeurIPS*, 2022.
- [21] Olaf Ronneberger, Philipp Fischer, and Thomas Brox. U-net: Convolutional networks for biomedical image segmentation. In *MICCAI*, volume 9351, pages 234–241. Springer, 2015.
- [22] Syed Waqas Zamir, Aditya Arora, Salman Khan, Munawar Hayat, Fahad Shahbaz Khan, and Ming-Hsuan Yang. Restormer: Efficient transformer for high-resolution image restoration. In *CVPR*, pages 5718–5729. IEEE, 2022.
- [23] Jiayi Ma, Pengwei Liang, Wei Yu, Chen Chen, Xiaojie Guo, Jia Wu, and Junjun Jiang. Infrared and visible image fusion via detail preserving adversarial learning. *Information Fusion*, 54:85–98, 2020.
- [24] Jiayi Ma, Han Xu, Junjun Jiang, Xiaoguang Mei, and Xiao-Ping (Steven) Zhang. Ddcgan: A dual-discriminator conditional generative adversarial network for multi-resolution image fusion. *IEEE Trans. Image Process.*, 29:4980–4995, 2020.
- [25] Hui Li and Xiao-Jun Wu. Densefuse: A fusion approach to infrared and visible images. *IEEE Transactions on Image Processing*, 28(5):2614–2623, 2018.
- [26] Hao Zhang and Jiayi Ma. Sdnet: A versatile squeeze-and-decomposition network for real-time image fusion. *Int. J. Comput. Vis.*, 129(10):2761–2785, 2021.
- [27] Xin Deng and Pier Luigi Dragotti. Deep convolutional neural network for multi-modal image restoration and fusion. *IEEE Trans. Pattern Anal. Mach. Intell.*, 43(10):3333–3348, 2021.
- [28] Fangyuan Gao, Xin Deng, Mai Xu, Jingyi Xu, and Pier Luigi Dragotti. Multi-modal convolutional dictionary learning. *IEEE Trans. Image Process.*, 31:1325–1339, 2022.
- [29] Shuang Xu, Zixiang Zhao, Yicheng Wang, Chunxia Zhang, Junmin Liu, and Jiangshe Zhang. Deep convolutional sparse coding networks for image fusion. *CoRR*, abs/2005.08448, 2020.
- [30] Han Xu, Jiayi Ma, Zhuliang Le, Junjun Jiang, and Xiaojie Guo. Fusiondn: A unified densely connected network for image fusion. In *AAAI Conference on Artificial Intelligence, AAAI*, pages 12484–12491, 2020.
- [31] Hao Zhang, Han Xu, Yang Xiao, Xiaojie Guo, and Jiayi Ma. Rethinking the image fusion: A fast unified image fusion network based on proportional maintenance of gradient and intensity. In *AAAI*, pages 12797–12804. AAAI Press, 2020.
- [32] Yu Zhang, Yu Liu, Peng Sun, Han Yan, Xiaolin Zhao, and Li Zhang. IFCNN: A general image fusion framework based on convolutional neural network. *Inf. Fusion*, 54:99–118, 2020.
- [33] Hyungjoo Jung, Youngjung Kim, Hyunsung Jang, Namkoo Ha, and Kwanghoon Sohn. Unsupervised deep image fusion with structure tensor representations. *IEEE Trans. Image Process.*, 29:3845–3858, 2020.
- [34] Man Zhou, Keyu Yan, Jie Huang, Zihe Yang, Xueyang Fu, and Feng Zhao. Mutual information-driven pan-sharpening. In *CVPR*, pages 1788–1798. IEEE, 2022.
- [35] Yiming Sun, Bing Cao, Pengfei Zhu, and Qinghua Hu. Detcfusion: A detection-driven infrared and visible image fusion network. In *ACM Multimedia*, pages 4003–4011, 2022.
- [36] Zhanbo Huang, Jinyuan Liu, Xin Fan, Risheng Liu, Wei Zhong, and Zhongxuan Luo. Reconet: Recurrent correction network for fast and efficient multi-modality image fusion. In *European Conference on Computer Vision (ECCV)*, 2022.
- [37] Dongdong Chen, Mike E. Davies, Matthias J. Ehrhardt, Carola-Bibiane Schönlieb, Ferdia Sherry, and Julián Tachella. Imaging with equivariant deep learning: From unrolled network design to fully unsupervised learning. *IEEE Signal Process. Mag.*, 40(1):134–147, 2023.
- [38] Dongdong Chen, Julián Tachella, and Mike E. Davies. Robust equivariant imaging: a fully unsupervised framework for learning to image from noisy and partial measurements. In *CVPR*, pages 5637–5646. IEEE, 2022.
- [39] Dongdong Chen, Julián Tachella, and Mike E. Davies. Equivariant imaging: Learning beyond the range space. In *ICCV*, pages 4359–4368. IEEE, 2021.
- [40] Julián Tachella, Dongdong Chen, and Mike Davies. Sensing theorems for unsupervised learning in linear inverse problems. *Journal of Machine Learning Research*, 24(39):1–45, 2023.

- [41] Weiwei Xu, Vincenzo Lipari, Paolo Bestagini, Politecnico di Milano, Wenchao Chen, and Stefano Tubaro. Equivariant imaging for self-supervised regularly undersampled seismic data interpolation. In *SEG International Exposition and Annual Meeting*, page D011S100R003. SEG, 2022.
- [42] Yiwei Chen, Chen Jiang, and Yu Pan. Single-photon image super-resolution via self-supervised learning. In *ICASSP 2023-2023 IEEE International Conference on Acoustics, Speech and Signal Processing (ICASSP)*, pages 1–5. IEEE, 2023.
- [43] Julián Tachella, Dongdong Chen, and Mike Davies. Unsupervised learning to solve inverse problems: Application to single-pixel imaging. In *Proceedings of the XXVIIIème Colloque Francophone de Traitement du Signal et des Images (GRETSI)*, September 2022.
- [44] Kaiming He, Xiangyu Zhang, Shaoqing Ren, and Jian Sun. Deep residual learning for image recognition. In *Conference on Computer Vision and Pattern Recognition, CVPR*, pages 770–778, 2016.
- [45] Linfeng Tang, Jiteng Yuan, Hao Zhang, Xingyu Jiang, and Jiayi Ma. Piafusion: A progressive infrared and visible image fusion network based on illumination aware. *Inf. Fusion*, 83-84:79–92, 2022.
- [46] Alexander Toet and Maarten A. Hogervorst. Progress in color night vision. *Optical Engineering*, 51(1):1 – 20, 2012.
- [47] Jiayi Ma, Yong Ma, and Chang Li. Infrared and visible image fusion methods and applications: A survey. *Information Fusion*, 45:153–178, 2019.
- [48] Glenn Jocher. ultralytics/yolov5. <https://github.com/ultralytics/yolov5>, October 2020.
- [49] Liang-Chieh Chen, Yukun Zhu, George Papandreou, Florian Schroff, and Hartwig Adam. Encoder-decoder with atrous separable convolution for semantic image segmentation. In *ECCV*, pages 833–851. Springer, 2018.
- [50] Harvard Medical website. <http://www.med.harvard.edu/AANLIB/home.html>.